Journal of Applied Electrochemistry (2005) 35:1045–1050
DOI 10.1007/s10800-005-9043-5

Synthesis and electrochemical behaviour of tin oxide for use as anode in lithium rechargeable batteries

A. SIVASHANMUGAM[1], T. PREMKUMAR[1], S. GOPUKUMAR[1,*], N. G. RENGANATHAN[1]
M. WOHLFAHRT-MEHRENS[2] and J. GARCHE[2]
[1]*Central Electrochemical Research Institute, Karaikudi, 630 006, India*
[2]*Center for Solar Energy and Hydrogen Research, Ulm, D-89081, Germany*
*(*author for correspondence, fax: +91-4565-227779; e-mail: deepika_41@rediffmail.com)*

Received 11 May 2004; accepted in revised form 24 November 2004

Key words: irreversible capacity, Li–Sn alloy, lithium battery anode, tin oxide anode

Abstract

SnO_2 was synthesized by precipitation from an aqueous solution of $SnCl_4$ and NH_4OH, followed by a heat treatment. The product was characterized by XRD, SEM, FTIR spectroscopy, DSC and TG. The XRD patterns suggest the formation of phase-pure cassiterite form of SnO_2. SEM imaging indicates that the particles obtained are of sub-micron size with good morphology and size control (around ~300 nm). Electrodes were fabricated by a slurry-coating procedure and the electrochemical performances of these electrodes were evaluated using galvanostatic cycling tests. The results suggest that the heat treated SnO_2 samples deliver higher capacities when cycled between 1.0 and 0.1 V vs. Li^+/Li and showed coulombic efficiencies of more than 98% in the tenth cycle.

1. Introduction

Although a number of primary cells based on metallic lithium are available in commerce, exploitation of lithium as an anode in secondary batteries is hampered by inherent dendrite growth upon recharge. Some interesting chemistries based on lithium metal anode and TiS_2 or MoS_2 cathode [1–3] appeared about two decades ago, but soon the limitations caught up with them. Since then lithium battery technology has witnessed immense changes not only in the choice of electrode materials and electrolytes, but also in concept and configuration. Lithium-ion cells can obviate safety problems associated with lithium dendrites during extended cycling. Lithium in these systems is sourced from lithiated transition metal oxide cathodes such as $LiCoO_2$, $LiMn_2O_4$, etc. Today, these batteries power gadgets such as laptop computers and cellular phones where weight and volume are important considerations.

Carbonaceous anodes are the most exploited of alternative anode materials in lithium-ion batteries. While disordered carbons can give high initial lithium insertion capacities, they exhibit continuous capacity fade as well as large hysteresis in their cycling profiles. On the other hand, graphitic carbons are limited by their capacity, which is 372 mAh g^{-1} for perfectly graphitic structures [4]. In 1997 Fujifilm Celltec reported [5] the performance of secondary lithium-tin alloy anodes derived from amorphous oxide materials. The amorphous tin oxide materials act as active centers for lithium absorption and give reversible lithium insertion capacities of >600 mAh g^{-1}, or nearly twice that of state-of-the-art carbon based anodes. During the first charging, tin oxide is reduced to tin, which is dispersed a matrix of lithium oxide [6–9]. The metallic tin then reversibly reacts with lithium to form a variety of alloys, reaching a composition of $Li_{4.4}Sn$ at the highest lithium concentration [10]. However, volume changes by as much as 259% associated with these alloying and dealloying reactions induces mechanical disintegration of the electrode.

Tin dioxides obtained from different synthesis routes are described in the literature [11–16]. Different textures and microstructures of the products play an important role in their electrochemical behavior. The effect of volume changes can to some extent be minimized by adopting suitable procedures for the preparation of tin oxide with small particle size as well as methods of electrode fabrication. In this work, we report the results of our study on the electrochemical lithium insertion behavior of amorphous SnO_2 prepared by a precipitation technique. The effect of calcination temperature of the product on its electrochemical performance is also reported.

2. Experimental

Various synthesis procedures such as sol–gel [17], chemical vapour deposition [18], magnetron sputtering [19], evaporation of elemental metal tin in an oxidizing atmosphere [20] and ultrasonic spray pyrolysis [21] have been employed to prepare SnO_2 powders and films. In this work, we have employed a precipitation technique for obtaining sub-micron size SnO_2 particles. Figure 1 is a schematic representation of the synthesis procedure. $SnCl_4$ (Merck) and NH_4OH (Merck) were used as precursors. $SnCl_4$ was dissolved in distilled water. NH_4OH solution was added until the pH reached 9, whereupon milky white $Sn(OH)_4$ precipitated. The precipitate was filtered and dried in air for a few days. The dehydration process is accompanied by the formation of SnO_2. The dried mass was ground to a fine powder and heat treated in air at 400 or 800 °C for 5 h. The reactions may be written as

$$SnCl_4 + 4NH_4OH \longrightarrow Sn(OH)_4 + 4NH_4Cl \quad (1)$$

$$Sn(OH)_4 \longrightarrow SnO_2 + 2H_2O \quad (2)$$

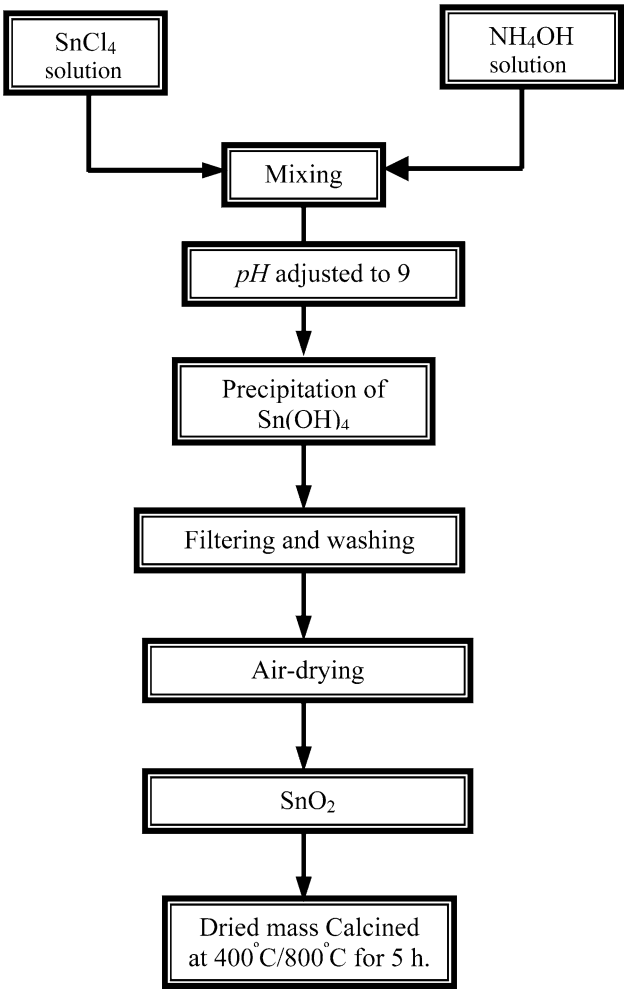

Fig. 1. A schematic diagram of the synthesis procedure for SnO_2.

The morphology of the products was examined by scanning electron microscopy (Zeiss, DSM 940, Germany) and the structural features were analyzed by X-ray diffraction (Siemens, D5000, Germany). Thermogravimetric and differential scanning calorimetric analyses were performed with 50–100 mg samples at a heating rate of 10 °C min^{-1} (Netzsch, STA 409, Germany). A Paragon 500 model Perkin Elmer (Germany) FTIR spectrophotometer was used for spectral analysis.

A typical three-electrode glass cell assembly was used for all electrochemical studies. The working electrode was made with SnO_2 powder, while a lithium foil (Merck) was used as counter and reference electrodes. The working electrode was prepared by a slurry-coating procedure. A slurry consisting of 85% SnO_2, 10% acetylene black and 5% polyvinylidene in ethylmethylketone was coated over a nickel foam tablet of 1 cm diameter. It was air-dried for a few minutes. Then the coated foam was enclosed in a nickel mesh packet and pressed under a 10 t load in a hydraulic press for a minute and vacuum-dried at 150 °C overnight. The nickel foam acted as the current collector for the working electrode. The electrolyte used was commercial LP 30 (Merck), a 1 M solution of $LiPF_6$ in a 1:1 (v/v) mixture of ethylene carbonate and diethyl carbonate. The electrodes were assembled in an argon-filled glove box (Mbraun, Germany) and cycled using a BEATE (Germany) cycling device between 1.0 and 0.1 V at 100-h rate for the first cycle and at 10-h rate for successive cycles. Ten cycles were performed.

3. Results and discussion

3.1. *Structure and morphology*

Figure 2 depicts the XRD pattern of the as-prepared and heat-treated SnO_2 samples. The peak positions fit well with standard values of the cassiterite phase of SnO_2 (JCPDS 41-1445). The XRD spectrum recorded for the as-prepared SnO_2 sample, shown in Figure 2(a)

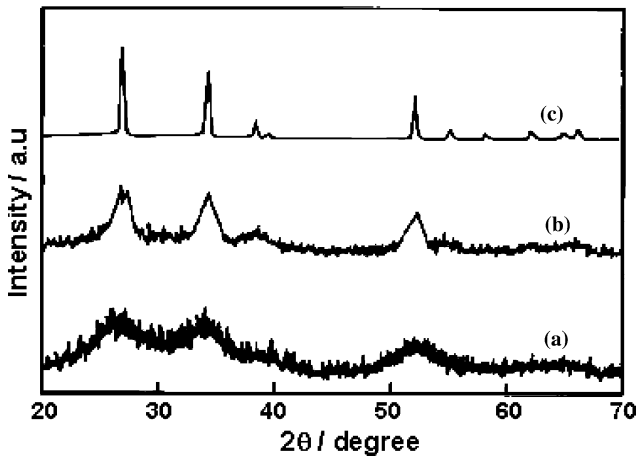

Fig. 2. XRD patterns of (a) as-synthesized, (b) SnO_2 calcined at 400 °C, and (c) SnO_2 calcined at 800 °C.

Table 1. Comparison of lattice parameters for SnO_2 samples with the standard values

Lattice parameter	Standard (Å)	Observed (Å)
a	4.7382	4.7099
c	3.1821	3.1516

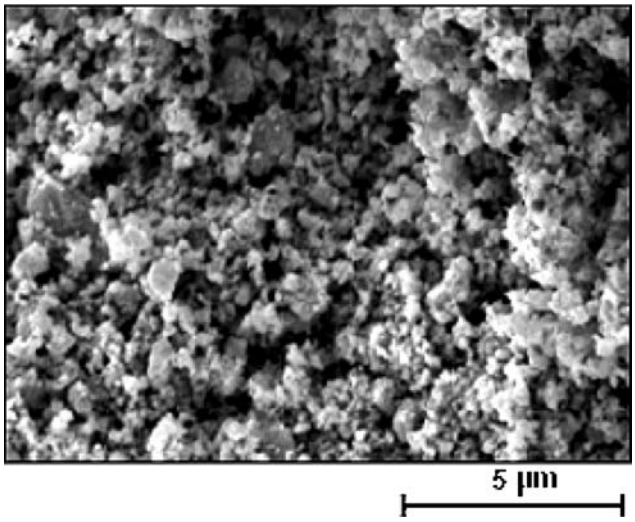

Fig. 3. A typical SEM image of SnO_2 (as-synthesized).

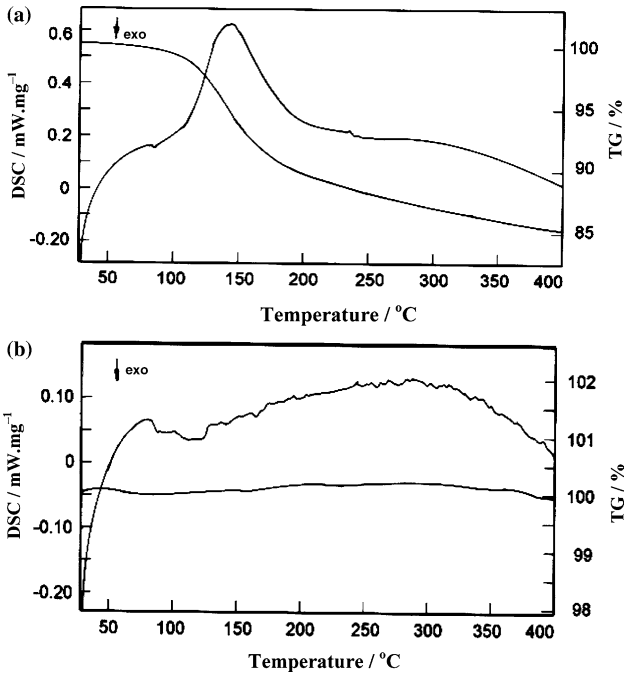

Fig. 4. TG and DSC curves of SnO_2: (a) as-synthesized (b) heated at 400 °C.

has broad peaks, which suggest that either the particles are very small crystallites or are semi-crystalline in nature [22]. The calculated values of the lattice parameters *a* and *c* are in good agreement with standard values (Table 1), which confirms the tetragonal structure of the synthesized SnO_2 powder. The XRD patterns of SnO_2 calcined at 400 and 800 °C for 5 h are presented in Figure 2 (b) and (c), respectively. It is seen that the reflections become gradually sharper with increasing temperature, indicating the larger crystallite sizes of the particles upon calcination. Thus, it appears that SnO_2 prepared by precipitation and subsequent heat treatment is a mixture of amorphous and crystalline particles. A typical SEM image of as-synthesized SnO_2 powder is given in Figure 3. It is clear from the image that the powder contains sub-micron sized particles with good morphology and size control. Particles of 200–300 nm size are seen to be present as agglomerates.

3.2. *Thermal analysis*

TG and DSC curves of the as-synthesized and heat treated (400 °C) tin oxide samples are presented in Figure 4 (a) and (b), respectively. The TG curve of the as-prepared sample shows a rapid weight loss of 11% between 100 and 200 °C, which is assigned to the dehydration process occurring along with the evaporation of physically adsorbed water and ammonia from the surface and pores of the particles. The dehydration process corresponds to a well-defined exothermic region in the DSC curve attributed to the formation of SnO_2. Beyond that and up to 400°C in the TG curve, there is only a slow weight loss region (1.88%), which may be attributed to the continuous removal of chemically adsorbed water related to the condensation of different types of surface hydroxyl groups [23]. However, no weight loss is observed in TG curve for the sample calcined at 400 °C [see Figure 4(b)]. The broad exothermic region in the DSC curve is attributed to the irreversible transition from the amorphous to crystalline state. This clearly shows that any bound water is completely removed during the 5-h calcination. In other words, a heat treatment of at least up to 400 °C is required to obtain a water-free product for use in lithium batteries.

3.3. *FTIR spectroscopy*

The FTIR spectra of the as-synthesized and heat-treated SnO_2 samples are presented in Figure 5. The spectrum of the as-synthesized SnO_2 exhibits an intense, broad peak between ~3600 and ~2500 cm^{-1}, with a maximum around ~3400 cm^{-1}, which may be due to adsorbed water and ammonia. The bands centered around ~1624 and ~1400 cm^{-1} are also related to water and ammonia. Expectedly, these peaks are absent in the spectra of the heat-treated samples [Figure 5 (b) and (c)]. The peak around 2350 cm^{-1} belongs to traces of residual CO_2 in the spectrophotometer's atmosphere, while the peaks at the low wave numbers (< 800 cm^{-1}) should be attributed to SnO_2. Two intense broad bands at ~658 and 573 cm^{-1} can be seen for the as-prepared SnO_2. However, the intensities of these peaks decrease upon calcination, with a new peak appearing at ~620 cm^{-1}. This band is assigned to the antisymmetric Sn–O–Sn stretching mode of the surface bridging oxide formed by

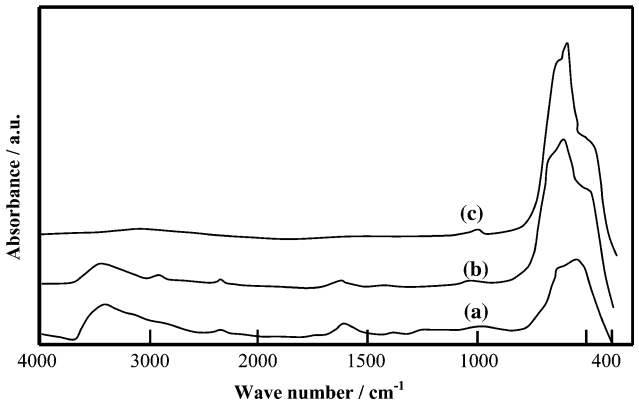

Fig. 5. FTIR spectra of SnO_2: (a) as-synthesized, (b) calcined at 400 °C, and (c) calcined at 800 °C.

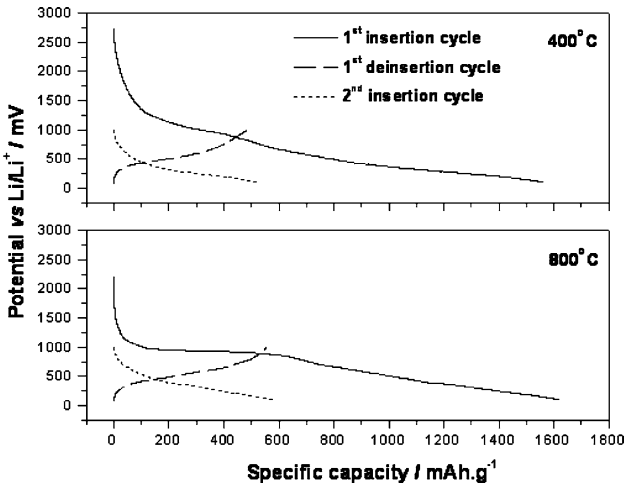

Fig. 6. Charge–discharge curves of SnO_2 heat treated at different temperatures.

the condensation of surface hydroxyl groups, yielding water. These spectral changes may be attributed to the changes in the size and shape of the SnO_2 particles, as have been demonstrated for SnO_2 particles of different sizes and shapes [23–25]. An increasing the calcination temperature results in a decrease in the intensity of the water band.

3.4. *Galvanostatic cycling*

Electrochemical lithiation of tin and tin-oxide electrodes involves several processes, viz., diffusion of Li^+ ions in the solution phase, Li^+ ion transfer across the solution/surface film interface and subsequent migration through the surface films, charge transfer by electrons (which compensates for charge in the alloying ions), solid-state diffusion of lithium into the bulk of SnO_2, and formation of various alloying phases. The degree of separation amongst these processes depends on the characteristics of the other constituent materials such as conducting material, binder, method of preparation of the electrode, orientation of the active mass and the characteristic time window of the experiment.

In the present study, the effect of calcination temperature on the active material is evaluated using galvanostatic cycling studies. The question of whether the amorphous or the crystalline tin oxide yields a higher capacity still remains unresolved with different workers reporting different results. According to Courtney and Dahn [7], tin-based composite oxides show high-capacity performance when they are comprised of amorphous structures. Nam et al. [26] subjected electron beam-evaporated thin films of SnO_2 to heat treatment up to 600 °C in air in order to understand the effect of heat treatment on the charge–discharge characteristics of SnO_2. However, the authors attributed the rapid loss in capacity with cycling to poor adhesion of the film to the substrate rather than to the amorphous or crystalline state of the active material [26]. Brousse et al. [8] reported high capacities over 100 cycles for SnO_2 films deposited by low-pressure chemical vapor deposition. Liu et al. [27] demonstrated high reversible capacities for heat-treated SnO_2 powders. According to the authors, heat treatment led to a more defined grain structure, which led to improved performance [27]. In our studies, we investigated the charge–discharge behaviour of SnO_2 calcined at 400 and 800 °C for 5 h. The charge–discharge curves of SnO_2 heat treated at 400 and 800°C are depicted in Figure 6. The first insertion regime was run from the open-circuit potential to 0.1 V; the first deinsertion and subsequent cycling were recorded between 1.0 and 0.1 V. The initial lithium insertion involves a irreversible reduction of tin oxide into metallic tin, while the subsequent cycles involve reversible alloying and dealloying of tin [6]. The reactions may be represented as follows:

$$4\ Li + 4\ e^- + SnO_2 \longrightarrow 2\ Li_2O + \ Sn \tag{3}$$

$$xLi^+ + xe^- + Sn \longleftrightarrow Li_xSn (0 \leq x \leq 4.4) \tag{4}$$

It can be seen from the Figure 6 that the first insertion profile of SnO_2 heat treated at 400 °C reflects a monotonic cathodic process with a weak plateau region around 1.0 V. A few more plateaus can also be seen. These signatures are well represented in the differential capacity curves depicted in Figure 7. The cycling data are presented in Table 2. The first-cycle insertion capacity for SnO_2 calcined at 400 and 800 °C are 1558 and 1618 mAh g^{-1}, respectively. The higher insertion capacity for the latter may be due to the better refined crystallinity of the sample, which provides easier pathways and necessary rearrangement of the constituent atoms. Furthermore, it is interesting to note that the first-cycle deinsertion capacities for SnO_2 heat-treated at 400 and 800 °C are 485 and 556 mAh g^{-1}, respectively. The higher deinsertion capacity obtained with the sample heat treated at 800 °C is attributed to the lower irreversible capacity which probably is due to smaller concentrations of surface hydroxyl groups.

Figure 7 shows the differential capacity curves of SnO_2 electrodes heat-treated at 400 and 800 °C for the first three scans, corresponding to the first-cycle inser-

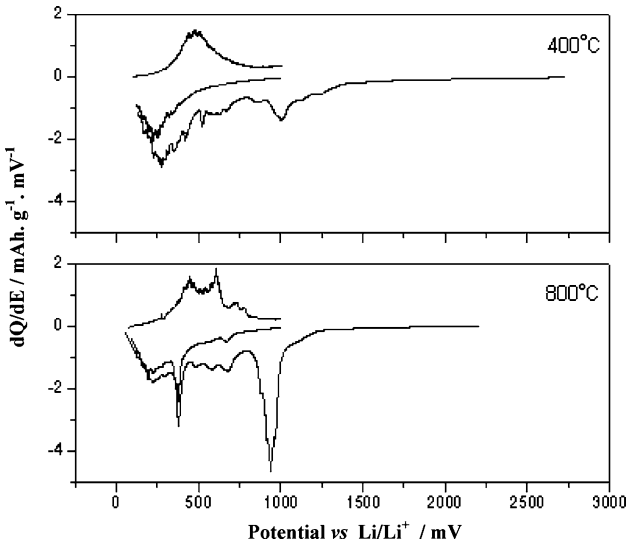

Fig. 7. Differential capacity curves of SnO_2 electrodes heat treated at different temperatures.

Table 2. Cycling data on heat treated SnO_2

Capacity data (mAh g^{-1})	400 °C	800 °C
Irreversible capacity	1073	1062
Deinsertion capacity in the 1st cycle	485	556
Deinsertion capacity in the 5th cycle	450	552
Deinsertion capacity in the 10th cycle	433	513
Capacity fade (mAh $cycle^{-1}$)	5.2	4.3

tion, first-cycle deinsertion and second-cycle insertion. There is a substantial difference in the profiles of the heat-treated samples. In the case of SnO_2 heat-treated at 400 °C, two cathodic peaks are observed during the first insertion cycle. The peak around 1.0 V may be assigned to the formation of Li_2O corresponding to the Equation (3). This reaction being irreversible, the peak does not appear in subsequent cycles. The formation of Li_2O in the first cycle leads to a large irreversible capacity. A small shoulder observed around 0.6 V and a broad peak extending to 0.1 V, and centered at 0.25 V, are ascribed to the formation of different alloy phases corresponding to the Equation (4). Even though the charging processes involve the formation of different Li–Sn alloy phases at different voltages, leading ultimately to a phase with a lithium stoichiometry of 4.4, there are no defined peaks corresponding to these alloy phases. In fact, the broad peak indicates that the necessary rearrangements of the constituent atoms to nucleate the various phases of Li–Sn alloys does not readily taking place due probably to kinetic reasons. It is suggested that the formation of the alloy phases take place on the outer surface of the electrodes even before they happen in the bulk. Lithium must, therefore, diffuse into the bulk for the various phases to develop. The process is semi-infinite diffusion-controlled, and hence appears like a single-phase transformation over a wide range of compositions. A well-defined broad peak is observed around 0.5 V during the deinsertion, corresponding to the discharge process, i.e., delithiation of the Li–Sn alloys. The major peak potential region, which lies between 0.3 and 0.7 V, corresponds to the potentials for the various Li–Sn alloy phases. While comparing the anodic and cathodic peaks in the above potential range, the cathodic side is less defined than is the anodic side. This suggests that the de-alloying process is more facile than the alloying process.

It is interesting to observe the changes on the signature peaks with the SnO_2 heated at 800 °C. The peak around 1 V, corresponding to the formation of Li_2O, is well-defined and predominant. This indicates more refined formation of the Li_2O matrix, which essentially facilitates a fine dispersion of the formed tin nanoparticles within Li_2O and allows easy diffusion of lithium inside the bulk of the electrode material. This is vindicated by the higher lithium insertion capacity in the first cycle. Furthermore, the better resolved peak signatures around 0.7, 0.6, 0.5, 0.4 and 0.2 V contrast with that of the single broad peak (centered at 0.2 V) noticed in the case of SnO_2 heated at 400 °C. These peaks may be attributed to certain Li–Sn alloy phases although the assignment of the peaks to individual alloy phases is not immediately obvious. In fact, our efforts to identify the alloy phases by *ex situ* XRD investigations on post-insertion electrodes in special holders at different insertion levels were not fruitful. It is evident from the better defined peaks that a relatively better environment persists for the insertion reaction in the case of crystalline materials. Similarly, in the deinsertion cycle also four peaks are seen around 0.4, 0.6 and 0.75 V. This again indicates that the de-alloying reactions are more facile than in the case with SnO_2 heated at 400 °C. It is suggested that the distinct peak signatures has to do with the crystallinity of the material that ensures the development of an ordered Li_2O matrix during the first insertion, which enables further reactions to proceed more efficiently.

Similarly, the SnO_2 sample heat-treated at 800 °C displayed a higher coulombic efficiency (more than 98%) (Figure 8). In Figure 9 the deinsertion capacities

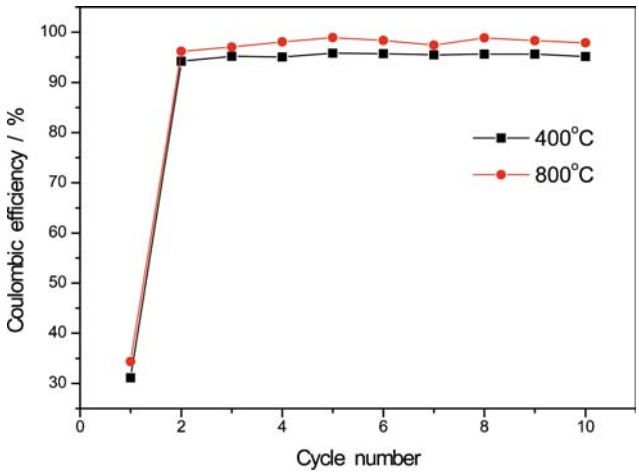

Fig. 8. Coulombic efficiency of SnO_2 electrodes heat treated at different temperatures.

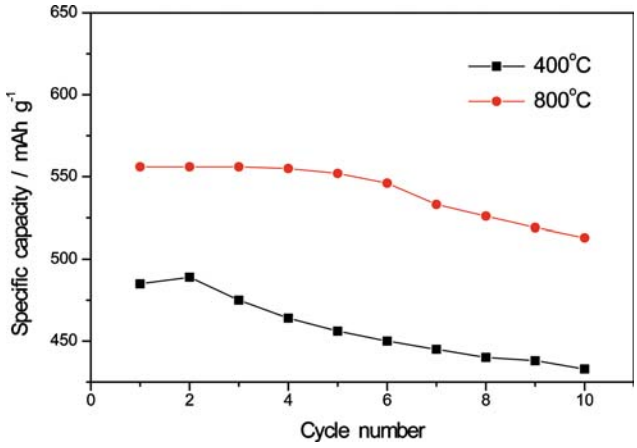

Fig. 9. Insertion capacity of SnO_2 heat-treated at different temperatures.

obtained in every cycle for SnO_2 heat treated at 400 and 800 °C are shown. Lithium dealloying is consistently superior for the more crystalline material, the SnO_2 sample heat treated at 800 °C. In the tenth cycle, SnO_2 calcined at 800 °C delivers 513 mAh g^{-1}while that calcined at 400°C delivers only 433 mAh g^{-1}. The better performance of SnO_2 calcined at 800 °C is in agreement with earlier observations [27–29] that SnO_2 with higher crystallinity displays good electrochemical performance.

4. Conclusions

Investigations on the lithium insertion–deinsertion properties and performance of SnO_2 powder derived from a precipitation technique were carried out for use as anode material in lithium ion battery. A slurry coating procedure over nickel substrate was adopted for the preparation of the electrodes. Based on the results we can conclude that the synthesized product is a phase pure SnO_2 material corresponding to cassiterite structure. Furthermore, highly crystalline SnO_2 calcined at 800 °C performs better than the samples heated at 400 °C in terms of reversible capacity and coulombic efficiency.

Acknowledgements

One of the authors (A.S.) thanks DAAD for offering a fellowship and also acknowledges the support and encouragement received from colleagues at ZSW, Ulm.

References

1. D.A. Winn, J.M. Shemilt and B.C.H. Steele, *Mater. Res. Bull.* **11** (1976) 559.
2. M.S. Wittingham, *Science* **192** (1976) 1444.
3. M.A. Py and R.R. Haering, *Can. J. Phys.* **61** (1993) 76.
4. T. Nagaura and K. Tazawa, *Prog. Batteries Sol. Cells* **9** (1990) 20.
5. Y. Idota, T. Kubota, A. Matsufuji, Y. Maekawa and T. Miyasaka, *Science* **276** (1997) 1395.
6. I.A. Courtney and J.R. Dahn, *J. Electrochem. Soc.* **144** (1997) 2045.
7. I.A. Courtney and J.R. Dahn, *J. Electrochem. Soc.* **144** (1997) 2943.
8. T. Brousse, R. Retoux, U. Herterich and P.M. Schleich, *J. Electrochem. Soc.* **145** (1998) 1.
9. J. Yang, M. Winter and J.O. Besenhard, *Solid State Ionics* **90** (1996) 281.
10. C.J. Wen and R.A. Huggins, *J. Electrochem. Soc.* **128** (1980) 1181.
11. T. Arai, *J. Phys. Soc. Jpn.* **15** (1960) 916.
12. B. Orel, U. Lavrencic-Stangar, Z.C. Orel, P. Bulkovec and M. Kosec, *J. Non-Cryst. Solids* **167** (1994) 272.
13. Y. Takahashi and Y. Wada, *J. Electrochem. Soc.* **137** (1990) 267.
14. S.R. Davis, A.V. Chadwick and J.D. Wright, *J. Mater. Chem.* **8** (1998) 2065.
15. C.V. Santilli, S.H. Pulcinelli, G.E.S. Brito and V. Briosis, *J. Phys. Chem. B.* **103** (1999) 2660.
16. R.C. Mehrotra, *J. Non-Cryst. Solids* **121** (1990) 1.
17. D. Wand, S. Wen, J. Chen, S. Zhang and F. Li, *Phys. Rev. B* **49** (1994) 14282.
18. R.D. Tarey and T.A. Raju, *Thin Solid Films* **128** (1995) 181.
19. T. Minami, H. Nanto and S. Takata, *Jpn. J. Appl. Phys.* **27** (1988) L287.
20. V. Schlosser and G. Wind, *in* Proceedings of 8th EC Photovoltaic Solar Energy Conf. Florence, Italy (1998) p. 998.
21. J. Lee and S. Park, *J. Am. Ceram. Soc.* **76** (1993) 777.
22. H. Klug and L. Alexander, *X-Ray Diffraction Procedure* (Wiley, New York, 1962), pp. 125.
23. P.G. Harrison, N.C. Lloyd, W. Daniell, C. Bailey and W. Azelee, *Chem. Mater.* **11** (1999) 896.
24. P.G. Harrison and A.J. Guest, *J. Chem. Soc. Faraday Trans.* **83** (1987) 3383.
25. J. Zhu, Z. Lu, S.T. Aruna, D. Aurbach and A. Gedanken, *Chem. Mater.* **12** (2000) 2557.
26. S.C. Nam, Y.H. Kim, W.L. Cho, B.W. Cho, H.S. Chun and K.S. Yun, *Electrochem. Solid State Lett.* **2** (1999) 9.
27. W. Liu, X. Huang, Z. Wang, H. Li and L. Chen, *J. Electrochem. Soc.* **145** (1998) 59.
28. J.H. Harreld, J. Sakamoto and B. Dunn, *J. Power Sources* **115** (2003) 19.
29. R. Zhang, J.Y. Lee and Z.L. Liu, *J. Power Sources* **112** (2002) 596.